ORIGINAL ARTICLE

Facile synthesis of strontium selenide supported copper sulfide hybrid nanosheets as an efficient electrode for high-performance OER

Ali Junaid[1] · Muhammad Abdullah[2] · Nigarish Bano[1] · Faiqa Noreen[1] · Syed Imran Abbas Shah[1] · Razan A. Alshgari[1] · Saikh Mohammad[3] · Sumaira Manzoor[1] · Muhammad Fahad Ehsan[4] · Muhammad Naeem Ashiq[1]

Abstract

To drive clean and sustainable fuel production via water electrolysis, development of high-performing, cost-effective electrocatalysts rich in earth elements without relying on precious metals or costly materials is crucial. In this study, strontium selenide (SrSe), copper sulfide (CuS), and composite SrSe@CuS via a traditional coprecipitate method under alkaline conditions are synthesized. Characterization techniques including X-ray diffraction, Transmission electron microscopy, Field emission scanning electron microscopy, and Brunauer–Emmett–Teller surface area analysis are employed to analyze the structure, morphology, and surface characteristics. The larger surface area of 123 $m^2\,g^{-1}$ and lower crystalline size (46.43 nm) of SrSe@CuS nanosheets show more active sites for oxygen evolution reaction. The oxygen evolution activity displayed overpotentials of 290 mV, a lower tafel slope of 67 mV dec^{-1}, and Lower charge transfer resistance (RCT) values of SrSe@CuS nanosheets (1.82 Ω) surpassing the individual SrSe and CuS nanosheets. Notably, the SrSe@CuS nanosheets exhibited remarkable stability, maintaining an oxygen evolution reaction (OER) activity of 10 mA cm^{-2} for over 50 h and sustaining a negligible loss in performance even after 50,000 cycles of repetitive cyclivoltammetry scans. These findings highlight their potential applicability in energy conversion and storage systems.

Graphical abstract
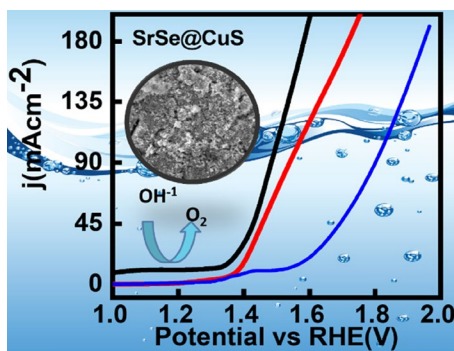
1 Introduction

The current era grapples with the challenge of soaring fossil fuel costs, surging demands, and limitations on alternative energy sources [1]. Meeting the escalating energy demands

Extended author information available on the last page of the article

in a rapidly growing world while maintaining environmental integrity has become paramount. The exponential rise in energy consumption since the Industrial Revolution demands an urgent shift to renewable energy sources [2]. This is the driving force behind efforts to develop renewable energy sources [3]. The extensive use of non-renewables like
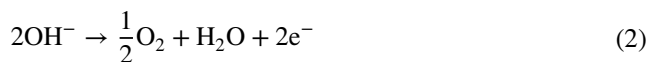
natural gas, petroleum, and their byproducts has intensified pollution and resource depletion, impacting global climate, economy, and society [4]. Unlike non-renewables, renewable resources offer advantage of reusability and minimal environmental impact [5]. For global efficacy, renewable energy must meet several criteria. Hydroelectric power, serving approximately one-third of the global population, is one such renewable energy source [6]. Geothermal power harnesses naturally occurring elements, offering a sustainable energy alternative [7]. While solar power exhibits enormous potential, climate variability and reduced sunlight in some regions pose limitations [8]. The ongoing quest for renewable energy seeks to mitigate adverse environmental effects of fossil fuels, ultimately striving to meet global energy needs sustainably.

Hydrogen (H_2) has emerged as a promising sustainable energy source, serving as a potential replacement for depleting fossil fuels [9]. Although hydrogen does not exist as H_2 naturally on Earth, it is present in molecules combined with carbon and oxygen, such as water and hydrocarbons [10]. H_2 is highly sought after as a clean-burning, efficient fuel that produces water as its primary byproduct, presenting a significant energy reservoir. Water splitting is most eco-friendly method to produce hydrogen, a process achieved through different methods like electrochemical and photoelectrochemical water splitting [11]. Electrochemical water splitting is favored for its stability compared to photoelectrochemical methods, which rely on sunlight availability and are less consistent under varying weather conditions [12, 13]. Alkaline water electrolysis stands as a prominent method due to its simplicity in producing hydrogen compared to solid oxide and proton exchange membrane electrolysis [14]. Efficient electrocatalysts are crucial for progress of various renewable energy technologies such as solar cells, metal-air batteries, fuel cells, and H_2O splitting [15]. OER is a crucial and rate-limiting process within this spectrum, urging the quest for more efficient electrocatalysts to reduce activation energies and improve conversion efficiency [16, 17]. While precious platinum group metals (PGM) have been historically popular, their cost and limited lifespan hinder practical application. Thus, nonprecious metal oxides, hydroxides, phosphates, and various sulfides and selenides are being explored as alternative, cost-effective electrocatalysts for OER [18, 19]. Transition metal sulfides and selenides, in particular, are being studied for their stability in both acidic and alkaline environments at low costs [20]. Alkali water splitting involves complex reactions. Proton conductivity of sulfide groups enables robust protonic conductivity. In transition metal sulfides, porous structure allows various oxidation states of metal species to enhance their redox activity [21]. General equations for the alkaline water-splitting reactions are:

Anodic reaction:

$$2H_2O + 2e^- \rightarrow H_2 + 2OH^- \qquad (1)$$

Cathodic reaction:

$$2OH^- \rightarrow \frac{1}{2}O_2 + H_2O + 2e^- \qquad (2)$$

Overall reaction:

$$H_2O \rightarrow H_2 + \frac{1}{2}O_2 \qquad (3)$$

Selenides in reported studies have been quite effective in carrying out OER, as demonstrated by previous studies, for example Nisa at el. manufactured $CdSe@SnO_2$ which demonstrated good catalytic performance and remarkable stability of water splitting. Electrocatalytic results of $CdSe@SnO_2$ Composites demonstrate a shorter overpotential of 233 mV to achieve current density of 10 mA cm^{-2} along with a low Tafel slope 89 mV dec^{-1} [22]. Abid et al. synthesized NiS@CeS by solvothermal production for Ni and Ce-based NiS@CeS supported on stainless steel (SSS) and compare OER activity of NiS@SSS, CeS@SSS, and their NiS@CeS@SSS electrodes. The electrocatalytic results of NiS@CeS composite exhibit low overpotential of 289 mV to achieve the current density of 10 mA cm^{-2} along with a small Tafel slop of 40 mV dec^{-1} [23]. Chen synthesis NiS by solvothermal method to fabricate NiS as effective H_2O splitting catalysts. Electrocatalytic results of NiS display unique overpotential of 279 mV to attain current density of 100 mA cm^{-2} along with a Tafel slope of 38.44 mV dec^{-1} [24]. Sun et al., successfully synthesized a bifunctional electrocatalyst, $MnS_xSe_{1-x}@N,F$-CQDs, through selenium anion substitution in manganese sulfide. This catalyst exhibits remarkable electrocatalytic performance for water splitting in alkaline solutions, demonstrated by low overpotentials (209 mV for OER at 10 mA cm^{-2}) and a low Tafel slope (72.18 mV dec^{-1}), showcasing its potential for efficient OER [25]. Wang et al., developed a durable oxygen evolution electrocatalyst, $FeSe_2@CoSe_2@NSC$, with exceptional performance in alkaline media, featuring a low overpotential of 278 mV at 10 mA cm^{-2} and a favorable Tafel slope of 53.08 mV dec^{-1} [26]. Wang et al., synthesized a high-performance oxygen evolution reaction (OER) catalyst, $NiCo_2Se_4@NiCoS_4$ heterostructure, showcasing remarkable efficiency. The catalyst exhibited a low overpotential of 248 mV at 10 mA cm^{-2} for OER, along with superior long-term stability and a reduced Tafel slope of 98.5 mV dec^{-1}, indicating its potential for OER applications [27]. Yang et al. created a highly-efficient OER catalyst using metal–organic framework-derived $FeS_2@CoNiSe_2$ nanosheets. The catalyst demonstrated exceptional OER performance with a low overpotential of 230 mV at

10 mA cm^{-2}, a modest Tafel slope of 54 mV dec^{-1} in 1 M KOH, and robust durability lasting up to 45 h, highlighting its promise for sustainable electrocatalysis [28]. All metal chalcogenide composites listed above performed exceptionally well, as well as exhibited extraordinary stability [29]. Metal sulfides and metal selenides are compounds in which a metal element is bonded to sulfides or selenium, respectively [30]. They have distinct colors, are commonly used as metal ores, and have various applications in industries such as mining, semiconductors, and pigments [31]. They can exhibit different electrical conductivities and undergo chemical reactions.

The novelty of copper sulfide (CuS) for the electrochemical oxygen evolution reaction (OER) stems from its earth-abundant and cost-effective nature. With diverse crystal structures, tunable properties, and photocatalytic potential, CuS offers versatility for customization and optimization. Synergistic effects with other materials, surface engineering strategies, and structural stability under OER conditions further enhance its electrocatalytic performance. Strontium selenide's electronic structure and band alignment can influence its catalytic activity for the OER. The stability of SrSe under OER conditions and its long-term durability are critical factors. A novel catalyst would ideally demonstrate robust performance over extended cycles. Combining strontium selenide with other materials or creating hybrid structures such as SrSe@CuS will lead to synergistic effects, enhancing overall catalytic performance.

The SrSe@CuS electrocatalyst for OER process was produced in this study using a straightforward coprecipitate method. Physical characterizations X-ray diffraction, Transmission electron microscopy, Field emission scanning electron microscopy, and Brunauer–Emmett–Teller was utilized to examine structure, lattice distance, morphology, and surface area of CuS, SrSe, and SrSe@CuS. These manufactured electrocatalysts demonstrated outstanding electrochemical performance when tested in a 1.0 molar potassium hydroxide electrolyte. The feasibility of mass-producing SrSe@CuS electrode material for use in oxidation reactions oxygen evolution reaction (OER) has not yet been investigated. Experiments in electrochemistry demonstrate that a current density of 10 mA cm^{-2} yields an small overpotential of 290 mV with a low Tafel slope value of 67 mV dec^{-1}. This study not only emphasizes the value of naturally occurring low-cost, high-yield catalysts, but it also surfaces the circumstances for further investigation of OER electrocatalysis.

2 Methodology

2.1 Materials

All of the chemical reagents utilized in these researches were got from various sources such as potassium sulfide (K$_2$S) 99% was purchased from Pubchem and the strontium nitrate (Sr(NO$_3$)$_2$ 98% and Cu(NO$_3$)$_2$·6H$_2$O (99%), selenium powder (99.99%) was purchased from Sigma Aldrich. Ethanol (C$_2$H$_5$OH) (99%) and deionized water obtained from Merck.

2.2 Synthesis of SrSe

Co-precipitation synthesis of strontium selenide (SrSe), was carried out using 0.5 M (10.56 g) strontium nitrate (Sr(NO$_3$)$_2$ dissolved in 100 mL of deionized water and selenium powder (reduced with hydrazine), after the adding of clean nickel foam (2 cm × 2 cm) and drying for eight hours at room temperature. To obtain SrSe nanosheets, NF was eliminated, washed with ethanol and DI water and dried of for 10 h at 80 °C. Then nanosheets was kept for further characterizations.
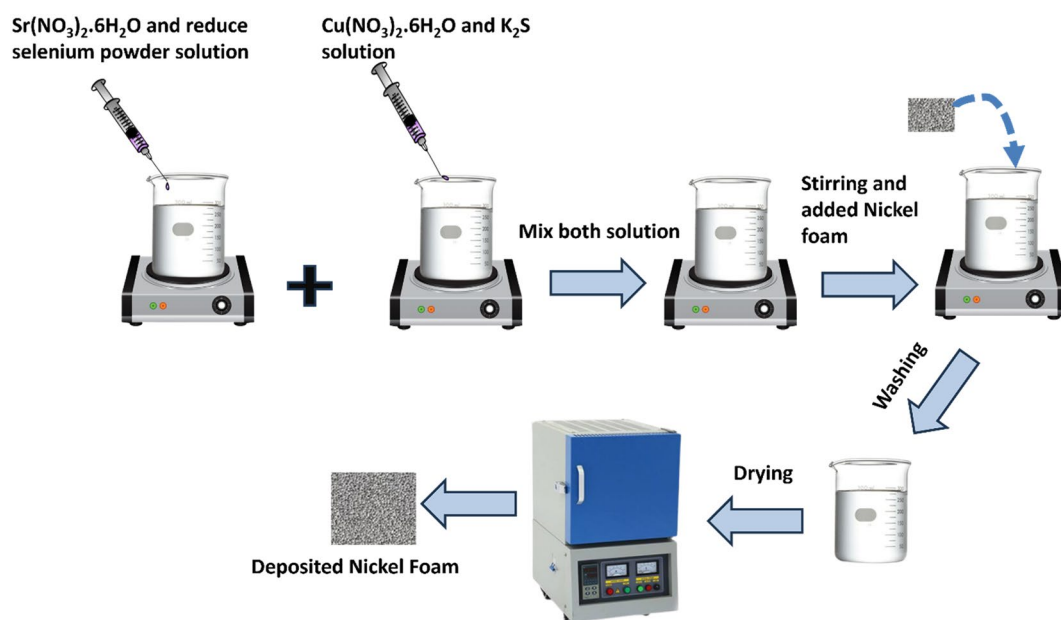
2.3 Synthesis of CuS

Copper Sulfide nanosheets were prepared by co-precipitation using DI water. For 15 min, we stirred a 0.5 M (14.75 g) Cu(NO$_3$)$_2$·6H$_2$O solution on a magnetic hot plate. Cu(NO$_3$)$_2$·6H$_2$O solution was added to 0.5 M (5.51 g) K$_2$S in 100 mL of DI H$_2$O through a burette with constant agitation. Then, clean nickel foam (2 cm × 2 cm) was placed and aged for 8 h at room temperature. To make CuS nanosheets, nickel foam was removed, cleaned with DI H$_2$O and ethanol, then dried at 80 °C for 10 h. Then nanosheets was kept for further characterizations.

2.4 Synthesis of SrSe@CuS

Co-precipitation was used to create SrSe@CuS nanosheets. Initial steps involved dissolving 0.5 M (10.56 g) Sr(NO$_3$)$_2$ in 50 mL of deionized water, before adding selenium powder that had been reduced with hydrazine and stirring to create a homogeneous solution (denoted A). Then, using a burette and constant agitation, 50 mL of DI H$_2$O was added to solution of 0.5 molar (14.75 g) Cu(NO$_3$)$_2$·6H$_2$O and 0.5 M (5.51 g) Potassium sulfide (K$_2$S) in DI water, obtaining a uniform solution (designated B). The cleaned nickel foam (2 cm × 2 cm) was immersed in a solution A/B mixture and Stirred for 8 h at room temperature. SrSe@CuS nanosheets were obtained after the nickel foam was removed, washed in DI H$_2$O and ethanol, and dried at 80 °C for 10 h. A detailed flowchart of the synthesis procedures is provided (Scheme 1).

2.5 preparation of NF for hydrothermal treatment

To prepare the electrode, NF was cut into small pieces of (2 cm × 2 cm). These pieces were subjected to sequential sonication in acetone, 2 M HCl, DI water, and ethanol

Scheme 1 Schematic representation for synthesis of SrSe@CuS

for 10 min each. The cleaned NF pieces were then dried for overnight at 60 °C in an oven. Nanomaterials were directly placed onto the NF substrate in electrochemical investigations.

2.6 Physical characterization

Powder XRD (Advance-D8 Bruker) with a Cu–k alpha radiation source ($\lambda = 1.541$ Å) was used to examine the crystal phase analysis of manufactured samples along the angle range of $2\theta = 25°$–$80°$ Debye-Scherer equation $D = \frac{0.9\lambda}{\beta\cos\theta}$ was utilized to approximate the size of the crystallites, where FWHM and are the full and half maximum diffraction intensities, respectively. Scanning electron microscopy (SEM) (using a Nova Nano SEM, 450) validated the morphology of the materials. Transmission electron microscopy (TEM) was used to inspect lattice distance. Brunauer–Emmett–Teller (BET) was handled with a Nova 2200e quantachrome analyzer at 77 K to examine the surface area of the materials.

2.7 Electrochemical characterization

The electrochemical findings were executed at room temperature using a 1.0 molar potassium hydroxide electrolyte and SrSe@CuS were used as the active electrodes. Electrochemical impedance spectroscopy (EIS), cyclic voltammetry (CV), linear sweep voltammetry (LSV), and chronoamperometry were all used to measure the electrocatalytic capacities of the samples. The CV and LSV curves were carried out in potential window of 1 V to − 1 V at a rate of 5 mV s^{-1}, and 0–1 V at scan rate of 5 mV s^{-1}, respectively. Reducing ohmic loss and getting rid of annoying background currents are two further applications. Each one of these calculations was performed with potential scale of SHE (standard hydrogen electrode). Electrode was pretreated with a 1:3 ratio of HNO_3 to HCl, then washed repeatedly with deionized H_2O and acetone, and finally dried at 60 °C.

2.7.1 Linear sweep voltammetry (LSV)

LSV is an electrochemical performance extensively used in water-splitting research to assess the electrocatalytic activity of materials involved in OER. LSV involves sweeping the working electrode's potential linearly while measuring the resulting current response in an aqueous electrolyte solution. It yields valuable information about the electrocatalyst's performance, including the onset potential for OER, Tafel slopes indicating reaction kinetics, insights into the reaction mechanism and evaluation of catalyst stability over multiple cycles. This data allows researchers to identify efficient electrocatalytic materials and optimize their design for the production of clean and sustainable H_2 through H_2O splitting [32].

2.7.2 EIS

In addition, EIS may be used to assess resistivity and conductivity [solution resistance (Rs) and Rct]. All EIS calculation were done at a potential of 0.5 V, a frequency of

1105 Hz, and an amplitude of 0.01. To determine the rate constant ($k°$), EIS might be used, as shown in Eq. 4.

$$K° = \frac{RT}{f^2 RctAC} \tag{4}$$

The constants for the global gas (8.314 J K^{-1} mol^{-1}), the thermodynamic temperature (298.15 K), the faraday constant (96,485 C mol), the Rct, the electrode surface area, and concentration of the electrolyte (1.0 M potassium hydroxide) are denoted as R, T, F, Rct, A, and C, respectively. Rapid electron transport occurs in an electrochemical event when k^0 is large.

2.7.3 ECSA

ECSA is also a crucial electrochemical efficiency parameter. CV polarization curves are utilized to determine this small potential window between 0 and 0.2 V outside of the faradic zone. For the non-faradic area of interest, CV polarization curves were collected at scan speeds of 10, 20, 30, and 40 mV s^{-1}. Using these polarization curves, we were able to calculate the Cdl. The Cs value (0.04 mF cm^{-2}) was then utilized to calculate the ECSA by dividing the acquired Cdl by the Cs of the smooth electrode, which is normally in the range (0.01–0.05 mFcm^{-2}) [29]. ECSA and roughness factor (fr) can be determined exhausting Eqs. (5) and (6) below.

$$ECSA = \frac{Cdl}{Cs} \tag{5}$$

$$fr = \frac{A2}{A1} \tag{6}$$

2.7.4 Stability of the electrode

Chronoamperometry and stability cycles both confirm electrocatalytic stability. During chronoamperometry, 50 h were spent subjecting the composite to a 0.7 V at constant applied potential.

3 Results and discussion

3.1 XRD

To regulate the crystal structure and the phase composition, XRD analysis was performed. Diffraction patterns of SrSe, CuS and a SrSe@CuS nanocomposite were scanned in 2θ range of 20°–80° is shown in Fig. 1. Both the pure CuS and SrSe peaks are in excellent agreement with corresponding standards from the JCPDS: 1-1281 (hexagonal, space group: P63mc) and 10-01-182 (monoclinic, space group:
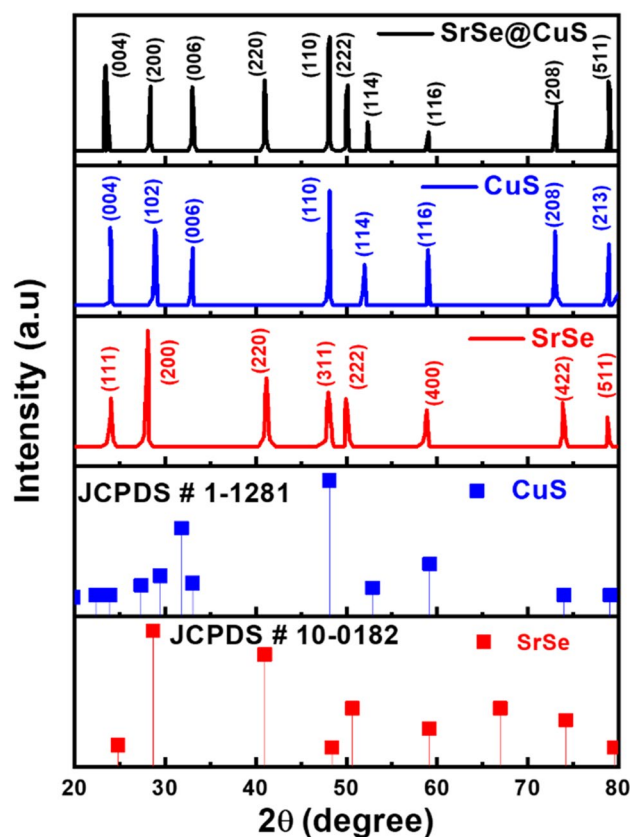
Fig. 1 XRD pattern of all grown products with their relevant standard pattern

P2/c), respectively. Figure 1 shows the XRD patterns of CuS nanosheets. The peaks at 23.01°, 28.9°, 33.05°, 48.09°, 52.31°, 59.01°, 74.92° and 78.71° in the XRD spectrum correspond to the planes (004), (102), (110), (114), (116), (208) and (213). The production of hexagonal polycrystalline CuS nanosheets is suggested by the fact that (110) diffraction signal is the strongest. It is feasible to determine that the structure is hexagonal by comparing the peak location in the XRD pattern to standard pattern of the hexagonal structure of CuS (JCPDS No. 1-1281). The patterns of the SrSe XRD are shown in Fig. 1. Strong peaks in the XRD pattern indicate that SrSe has crystallized. Most noticeable peaks are seen in the opposing cubic structure. Diffraction pattern of SrSe@CuS is shown in Fig. 1. The phases of SrSe and CuS (004), (200), (006), (220), (110), (222), (114), (116), (208), and (511) respectively, were linked to the strong peaks found at 23.31, 28.51, 33.05, 40.09°, 48.09°, 50.05°, 52.39°, 59.01°, 72.91°, and 78.89°. The principal diffraction peaks of the synthesized SrSe changed dramatically when a SrSe@CuS composite was made. Diffraction patterns are influenced by many factors, including shifts in crystal structure, variations in atomic size, possibility of phase transitions, and interactions between SrSe and CuS. Alterations seen

are indicative of nano-scale structural modifications due to composite synthesis.

To determine crystallite size, full width at half maxima (β) was determined, and using that Debye Scherrer formula: where (*hkl*) are miller indices, (λ) is the X-rays wavelength Cu-kα radiations (1.5406), (θ) is the angle of diffraction (Bragg angle) in degrees, (*k*) is a dimensionless measure known as the shape factor with a value of 0.9, is the result from fitting a Gaussian single peak to the data in Origin pro 9. The crystallite size of the CuS, SrSe, and SrSe@CuS nanosheets are 87.43, 74.86 and 46.43 nm, respectively.

The SEM images of SrSe@CuS (Fig. 2c, d) show that the nanocomposite developed on the Ni foams in a dense, vertical, and uniform pattern. Potential for effective OER is shown by a nanocomposite on Ni foams with a thick, vertical, and uniform pattern. This setup maintains constant catalytic activity, facilitates gas development, and offers a large surface area for catalysis. To learn more about the nanosheets, see Fig. 2b's high-magnification SEM photographs of them. The nanosheets had a thickness of around 7.8 nm, based on the SEM scans. Increased oxygen evolution may result from the capacity to expose more active sites to electrolytes while allowing electrons and ions to move quickly within such a thin framework [33]. In fact, SrSe@CuS nanosheets have structural similarities with their forerunner, which can be shown in Fig. 2a, b and is also made up of free-standing, vertically interacting SrSe and CuS nanosheets. Moreover, the TEM was investigated to analyze the internal structure of nanosheets of SrSe@CuS shown in Fig. 2e. The long resolution TEM in Fig. 2f indicate the presence of lattice fringes having lattice distance of 22.3 nm and 33.2 nm which corresponds to the (004 and 111) planes of CuS and SrSe, confirm the formation of composite SrSe@CuS. The generated CuS and SrSe nanosheets are spherical and evenly scattered, as seen by SEM images. The lab produced CuS and SrSe nanosheets that are extensively scattered and range in size from 13 to 20 nm, as seen by SEM micrographs. The SEM picture shows that the diameters and XRD values of the CuS and SrSe nanosheets are exactly in line with one another.

The BET technique was used to measured the specific pore size and surface area of the nanosheets in the N_2 adsorption–desorption isotherm. The isotherm of CuS, SrSe, and nanocomposite made of all three materials is shown in Fig. 3. The mesoporous nature of the synthesized CuS, SrSe, and SrSe@CuS nanosheets is shown by their association with the type IV profile of the adsorption–desorption isotherm. [34]. The measured surface area, pore diameters, and volumes of CuS, SrSe, and SrSe@CuS nanosheets are 49 m^2 g^{-1}, 70 m^2 g^{-1}, 123 m^2 g^{-1} 11.5 nm, 1.6 nm, and 4.1 nm, and 0.18, 0.25, and 0.78 cm^3 g^{-1}, separately. The BET surface area of SrSe@CuS is longer than those of EG@Ni$_3$Se$_2$ (29 m^2 g^{-1}) and EG@Co$_9$S$_8$ (37 m^2 g^{-1}) Since it is mesoporous, it has a large amount of exposed active sites, can transport and adsorb large amounts of mass, and therefore useful in electrochemical processes. The larger surface area of synthesized nanosheets allow for a greater number of catalytic active sites, leading to more efficient and effective OER processes [35]. As a result, the obtained material was a suitable electrocatalyst for OER.
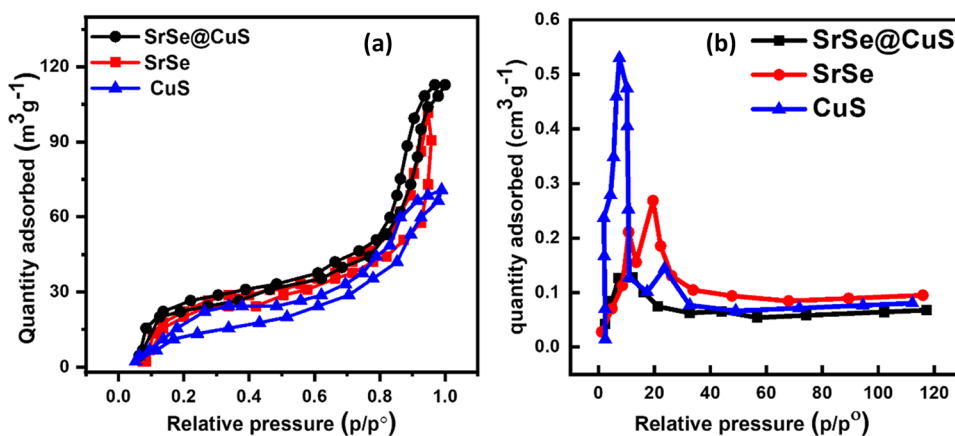
3.2 Electrochemical study

SrSe LSV was depleted to measure the CuS electrocatalytic OER activity in N-saturated 1 M potassium hydroxide at a scan rate of 10 mV s^{-1} (Fig. 4a). NF electrodes with and without catalysts, had their LSV profiles evaluated. Every polarization plot of the catalyst-equipped NF electrodes


Fig. 2 SEM analysis for **a** SrSe, **b** CuS, **c**, **d** SEM images of SrSe@CuS and **e**, **f** TEM and HRTEM images for SrSe@CuS
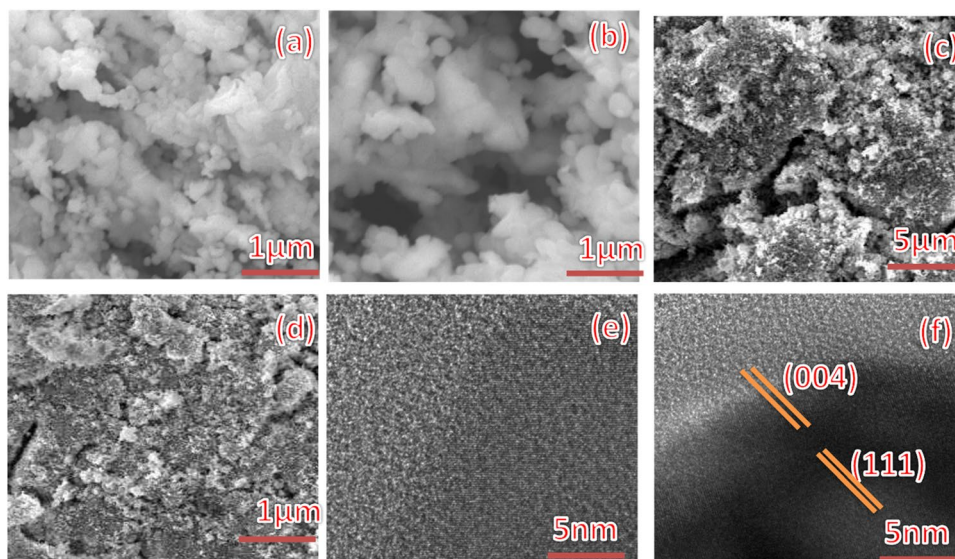
Fig. 3 **a** Adsorption–desorption isotherm of material in BET. **b** Pore-size distribution curve analysis for SrSe, CuS, SrSe@CuS

Fig. 4 Comparison of electrochemical; activity for OER activity **a** LSV curves, **b** Tafel slopes comparison, **c** electrochemical impedance spectroscopy, **d** normalized curve density SrSe, CuS, SrSe@CuS
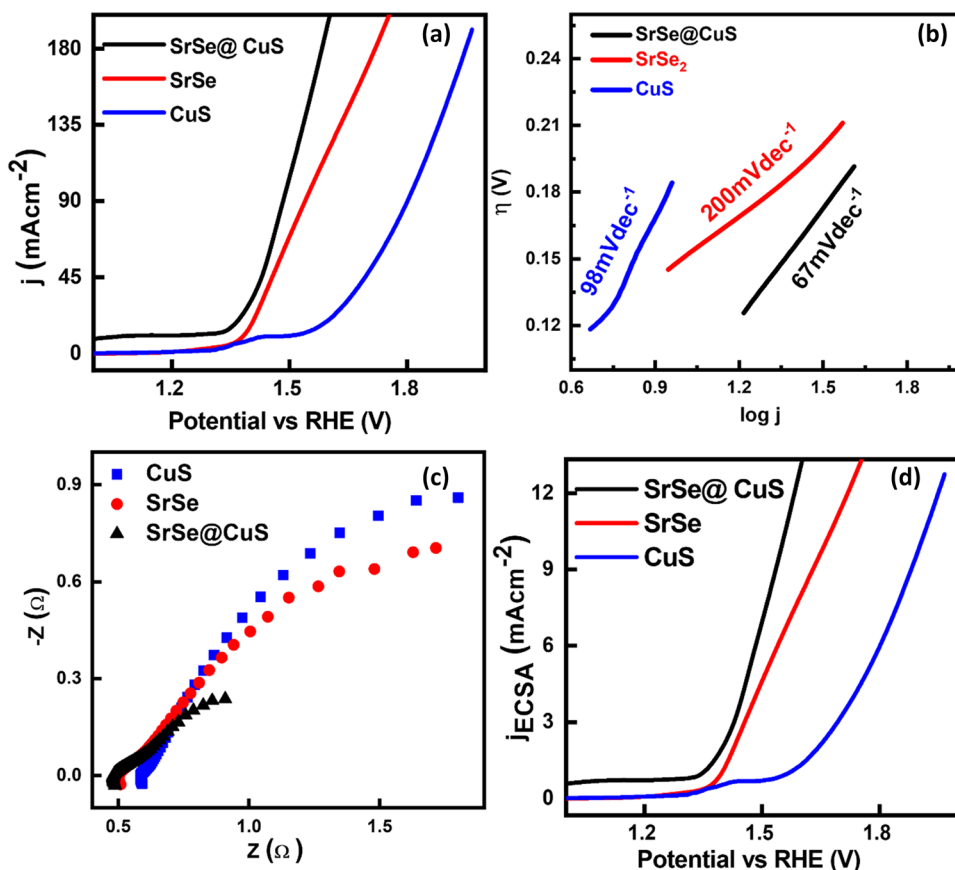
demonstrated a sharp rise in anodic current density at a given bias potential. This example illustrates how oxygen is produced at the electrode surface via electrochemical processes. The polarization graphs bear striking similarities to the known OER catalysts. In addition, the unaltered NF electrode's polarization pattern demonstrates that its current density is minuscule [36]. This highlights the worth of the catalyst in boosting OER at the surface of the improved electrode. Due to the fact that the OER current density was larger in SrSe@CuS than in pure CuS and SrSe, the

polarization plots demonstrate that SrSe considerably aids in enhancing OER activity [37]. This enhancement may be the result of catalytic synergy, increased active sites, altered surface properties, and possible electronic effects. Different developed catalysts have varying OER onset potentials. The SrSe@CuS catalyst had the small onset potential (the aptitude to produce a current density of 10 mA cm^{-2}) of the built-in catalysts. It is vital to remember that SrSe@CuS has lower OER onset potentials than standard IrO$_2$. SrSe@CuS can be used to separate water as a consequence. The
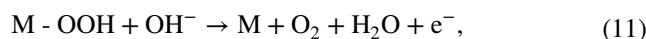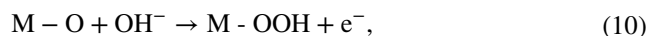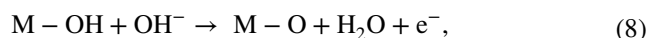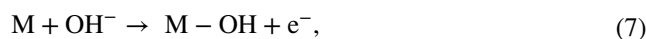
efficiency of an OER catalyst is commonly determined by the amount of overpotential mandatory to produce a current density of 10 mA cm^{-2}, which is respected to equate to a solar energy exchange productivity of 10% [38]. The overpotentials necessary for each of the catalysts utilized in this experiment to generate 10 mA cm^{-2}. SrSe@CuS had the smallest potential (0.29 V) and longest OER activity. The overpotential values needed to employ good OER catalysts like IrO$_x$ (0.32 V) and RuO$_2$ (0.32 V) and obtained 10 mA cm^{-2} current density from the catalysts during development were equivalent to (0.319 V). 310 mV overpotential is what Swesi et al. report after electroplating Ni$_2$Se$_3$ for 300 s. CoS$_2$@graphene composite made by solid-state thermolysis was found to have 380 mV overpotential[39]. In this instance, 10 mA cm^{-2} are produced by pure CuS and SrSe at 301 mV and 342 mV versus RHE, respectively. According to a study of a particular system using density functional theory, the electrical structure and atomic environment of the catalyst surface, especially the metal–oxygen bond strength, frequently change throughout the creation of a composite. In addition, it is proposed that the addition of SrSe to CuS alters the electrical environment on the surface, causing faults or enhancing contact between nearby Cu atoms. The OER has the lowest overpotential, the smallest Rct, and the longer electrochemically active surface area in this situation because SrSe enhances the conductivity of electrocatalysts.

Understanding how OER operates at the catalyst surface requires an understanding of the Tafel slope as well. The slope of the Tafel was determined using LSV plots. Figure 4b displays the Tafel diagrams for each sample. In every instance where slopes and log j were measured, a linear association was discovered. The Tafel slopes for pure CuS and SrSe@CuS were found to be 98 mV dec^{-1} and 67 mV dec^{-1}, respectively. By having the highest OER activity, which is often connected with the lowest Tafel slope value, SrSe@CuS outperformed other OER catalysts like IrO$_2$. After that, the reported SrSe@CuS OER's performance was contrasted with that of other CuS-based materials (EIS). The current between the electrode and electrolyte was determined using electrochemical impedance spectroscopy (EIS). Complex impedance map (Nyquist plot) is frequently employed to investigate charge transport over an electrochemical interaction [40]. Figure 4c displays a comparison between the Nyquist plots of pure CuS, SrSe, and SrSe@CuS. There was always a perfect high-frequency region in the shape of a line and a low-frequency region in the shape of a half circle. The length of the arc represents the electrode–electrolyte interface's Rct. A solution resistance (Rs), constant phase element (CPE), and Warburg impedance (Zw) were fashioned from the data to form a similar circuit. The measured R_{CT} value of CuS, SrSe, and SrSe@CuS nanosheets are 3.6, 3.4, 1.82 Ω, respectively. There is already a growing collection of Rct values for a wide variety of catalysts. There may

be an increase in charge transfer between the catalyst and electrolyte when Rct is low. Incorporating SrSe into the CuS structure enhances the kinetics of charge transfer, affecting the OER's kinetics. This is probably related to the improved electrical characteristics of the composite catalysts.

An oxygen evolution reaction catalyst's long-term stability affects how effective it is in practical applications [41]. Some compounds, especially IrO$_2$, have undergone chronoamperometry tests to ascertain their stability or durability. Standard chrono potentiometric studies were carried out in 1 M N$_2$-saturated KOH for 50 h at 0.7 V (versus RHE) and 1600 rpm RDE rotation rate. Within the first 10 min, it was discovered that the initial high OER current densities for all samples were decreasing. The SrSe@CuS had current densities of 7.05 mA cm^{-2}, 6.24 mA cm^{-2}, 3.78 mA cm^{-2}, and 2 mA cm^{-2} after 10 min and 50 h, respectively. This is because SrSe@CuS can withstand current densities of 88% better than any other electrocatalyst that has been tested. This is connected to the finding that multi metallic Ni–Mo@Cu nanowires maintained 86% of their OER current density after 12 h of amperometry testing. In addition, the catalyst could stray from the electrode, deteriorate with time, or come into contact with water droplets or bubbles that impede it. SrSe@CuS exhibited its high performance throughout the whole 50-h test, surpassing any other established electrocatalyst with regard of current density (Fig. 5).

Electrolysis of water is the use of an external voltage to separate H$_2$O into its component elements, H$_2$ and O$_2$. Electrode catalysts enhance both the water-splitting and OER processes, but the reaction pathway must first be determined. Low pH causes two water molecules to undergo OER, producing four protons and one oxygen molecule. When four OH$^-$ are oxidized to H$_2$O and O$_2$ in an alkaline medium, oxygen is generated. Researchers have examined OER in acidic and alkaline environments to postulate its likely processes. Oxygen evolution typically involved the adsorption and desorption of intermediate O^{-2} containing molecules on catalytically active sites. While the exact process of OER is still up for debate, the following stages have been postulated for alkaline solutions.

$$M + OH^- \rightarrow M - OH + e^-, \tag{7}$$

$$M - OH + OH^- \rightarrow M - O + H_2O + e^-, \tag{8}$$

$$2M - O \rightarrow 2M + O2 \text{ or,} \tag{9}$$

$$M - O + OH^- \rightarrow M - OOH + e^-, \tag{10}$$

$$M - OOH + OH^- \rightarrow M + O_2 + H_2O + e^-, \tag{11}$$

where M stands for the amount of electrocatalyst surface-active sites. At the beginning of oxygen evolution reaction,

Fig. 5 a Comparison of LSV curves before and after 20,000 CV cycles. **b** Chronoamperometry test in 1 M KOH solution
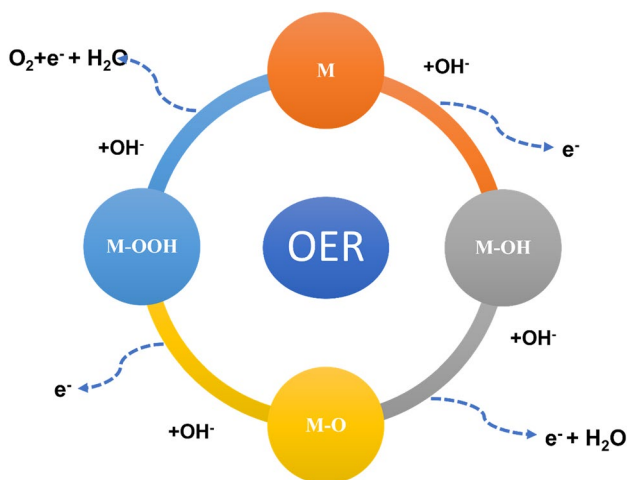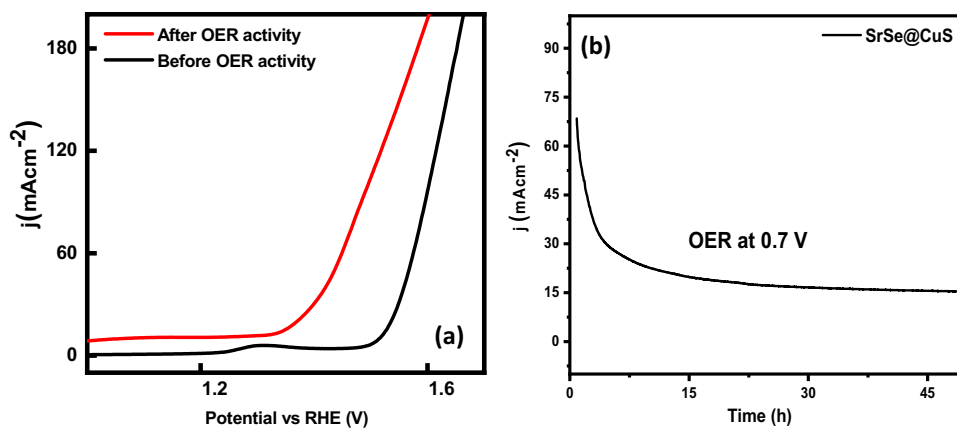
Scheme 2 Propose OER mechanism

OH$^-$ absorbed on the active site oxidize to M–OH. After then, M–OH loses a proton and e$^-$, changing into M–O. After that, M–O travels along one of two routes to become O$_2$ molecules (Scheme 2). Two M–O species mix and transform into O$_2$ and M active sites, for one thing. In contrast,

M–O converts to M–OH and a further proton-coupled electron transfer step, ultimately yielding O$_2$ [42].

The larger the ECSA the greater the catalytic activity. Since the electrochemical reaction takes place on the electrode's surface, an increase in ECSA results in more active sites for the catalytic process. Electrochemical double-layer capacitance (ECSA) analysis provided on the differences in electrocatalytic behavior of SrSe@CuS, SrSe, and CuS predecessors by measuring Cdl variations (Table 1). The technique explained the differences in catalytic activity by providing information on the materials' interactions with reactants. Figure 6 plots the scan rate vs the variation in the current density of the Cdl. Cdl values of 6.9 mF, 12.5 mF, and 13.4 mF were measured for CuS, SrSe, and SrSe@CuS, respectively. Similar ESCA values of 172.5, 312.5, and 335 are seen for CuS, SrSe, and SrSe@CuS. This illustrates the rate of expansion of active sites with an OER focus. Enhanced conductivity inside the composite structure might be responsible for the higher ECSA value of SrSe@CuS in comparison to SrSe and CuS, as may an increase in active sites, surface changes, and improved catalytic structures. All of these components work together to improve SrSe@CuS's electrochemical performance. The Rf of an electrocatalyst

Table 1 Comparative OER performance

Sample	Overpotential at 10 mA cm^{-2} (V)	Tafel slope (mv dec^{-1})	Activity	References
CuS/MnCO$_3$/NF	70 mV	42.5 mV dec^{-1}	OER	[43]
CoSe$_2$/FeSe$_2$	291 mV	62 mV dec^{-1}	OER	[44]
NiCo$_2$Se$_4$ and CoNi$_2$Se$_4$	257 and 244 mV	117 and 80 mV dec^{-1}	OER	[45]
NiS$_2$/NiSe$_2$	290 mV	119 mV dec^{-1}	OER	[46]
NiSe$_2$/FeSe$_2$	256 mV	50 mV dec^{-1}	OER	[47]
NiSe-Ni$_3$Se$_2$/MWCNT	325 mV	70.2 mV dec^{-1}	OER	[48]
Cu$_2$Se/NiSe$_2$	277 mV	40.17 mV dec^{-1}	OER	[49]
(Co$_4$Mn$_1$) Se$_2$	274 mV	39 mV dec^{-1}	OER	[50]
FeSe$_2$@CoSe$_2$/rGO	260 mV	36.3 mV dec^{-1}	OER	[51]
SrSe@CuS	290 mV	67 mV dec^{-1}	OER	Current study

Fig. 6 ECSA at different scan rate **a** SrSe, **b** CuS and **c** SrSe@CuS, Cdl plot profile of **d** SrSe, **e** CuS and **f** SrSe@CuS
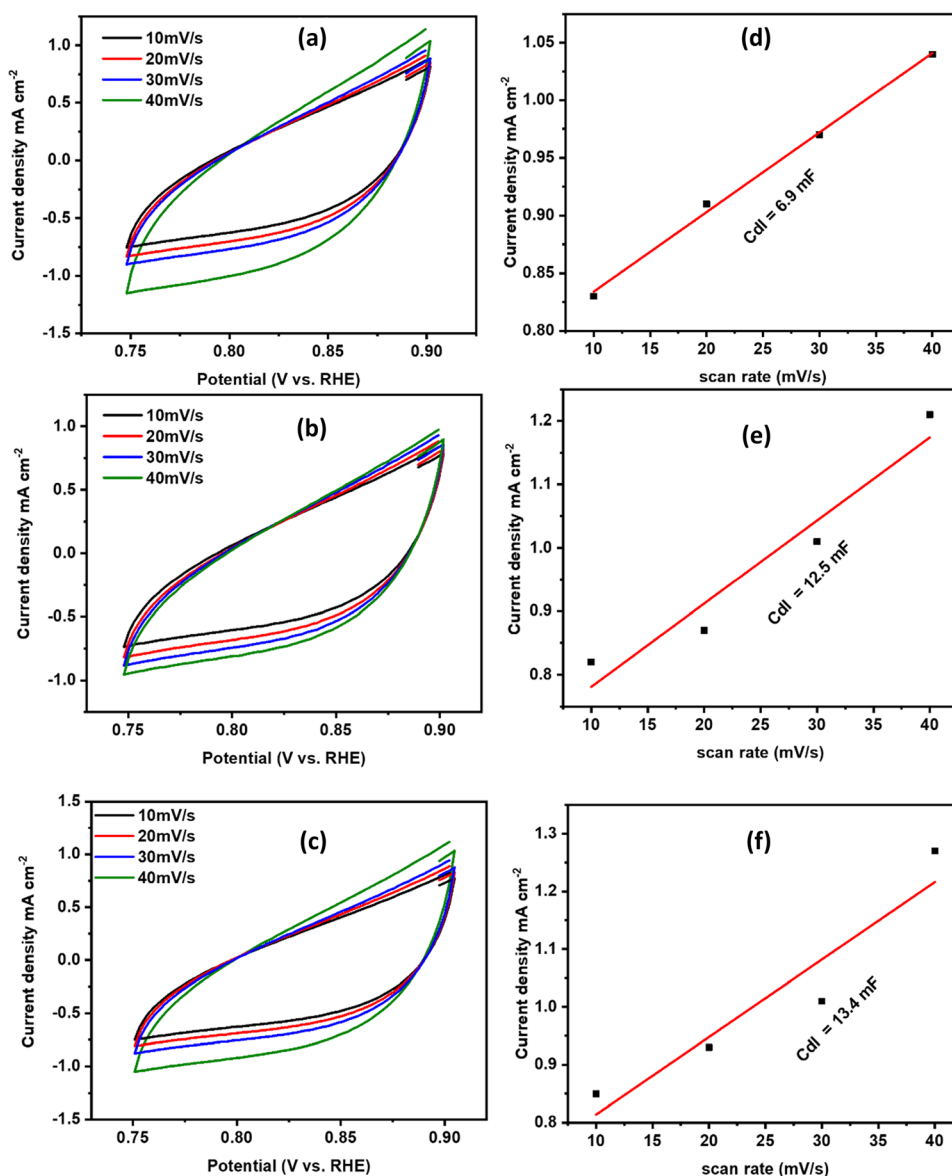
has a big effect on how well it works as an electrocatalyst (Rf). When Rf goes up, electrocatalytic activity goes up, and the same is true when Rf goes down. By adding the ECSA to the linear surface area of the electrode, the Rf values of several catalysts were found (0.5 cm^{-2}). Also, the Rf value of the SrSe@CuS catalyst was the highest of all the catalysts that were made. This discovery shows that SrSe@CuS works better as an OER catalyst than other materials. Because of synergistic effects, enhanced active sites, improved interfaces, and favorable electronic structures, SrSe@CuS has been shown to have better catalytic activity as an OER catalyst. These components work together to make water splitting more efficient because of the composite's superior performance in oxygen evolution. With the turnover rate of the catalyst, it is possible to figure out the oxygen evolution

reaction kinetics at an electrode surface (TOF). To figure out the TOF of the catalysts, it was assumed that each Cu and Sr (called a "catalytic site") was intricate in electrocatalysis when the catalysts were made in 1 molar KOH. The equation was used to figure out the TOF (12).

$$TOF = (Jg \times Sgeo)/(4 \times F \times n), \qquad (12)$$

where F is the Faraday constant (96,500 C mol^{-1}), Sgeo is the surface area of the NF electrode (0.2 cm^{-2}), Jg is the current density at an overpotential of 0.42 V, and n is the number of atomic moles of Cu and Sr in the electrode. Four electrons are given to each freshly formed O_2 molecule, hence n is thought to equal four [52]. The material's capacity to efficiently promote the reaction is reflected in the TOF

value, which is proportional to the OER rate per active site. The specific current density (Js) of catalyst during manufacturing was obtained by multiplying the observed current density at a predefined overpotential (0.42 V) by the roughness factor (R_f) (13).

$$R_f = ECSA/GSA \tag{13}$$

4 Conclusion

Hydrothermally synthesized SrSe@CuS nanocomposites were utilized for OER activity in hydrogen production in this investigation. XRD, SEM, TEM, and BET were used to study the structural, morphologic, lattice distance and surface area characteristics of the manufactured material. With a larger surface area of 123 m^2 g^{-1} and a smaller crystalline size of 46.43 nm, the SrSe@CuS nanosheets have more active sites, which increases their catalytic effectiveness in the oxygen evolution reaction. An electrochemical analysis revealed that the SrSe@CuS-based nanocomposite has a 290 mV overpotential and a low Tafel slope value of 67 mV dec^{-1}. ESCA values of 335 cm^2 are seen for SrSe@CuS that shows rate of expansion of active sites with an increased OER activity. SrSe@CuS nanosheets (1.82 Ω) have lower charge transfer resistance (RCT) values than CuS (3.6 Ω) and SrSe (3.4 Ω), indicating superior charge transfer efficiency. The enhanced functioning of the nanocomposite was attributable to the fabrication of a nanosheet-embedded CuS on SrSe structure with increased surface area and superior conductivity. Due to Cu and Sr's high-electron conductivity and highly reactive oxygen functional groups, the OER and the water-splitting reaction accelerate hydrogen production. Meanwhile, the SrSe@CuS catalyst showed excellent stability for 50 h or 50,000 cycles under alkaline conditions. Our findings indicate that the SrSe@CuS nanocomposite, which is novel and practical, has the highest OER activity and may be utilized in various energy-related devices.

Author contributions All have done equal contribution.

Data availability The datasets generated during and/or analysed during the current study are available from the corresponding author on reasonable request.

Declarations

References

1. A.W. Rennuit-Mortensen, K.D. Rasmussen, M. Grahn, How replacing fossil fuels with electrofuels could influence the demand for renewable energy and land area. Smart Energy **10**, 100107 (2023)

2. A. Zahoor et al., The carbon neutrality feasibility of worldwide and in China's transportation sector by E-car and renewable energy sources before 2060. J. Energy Storage **61**, 106696 (2023)

3. F.Z. Ainou, M. Ali, M. Sadiq, Green energy security assessment in Morocco: green finance as a step toward sustainable energy transition. Environ. Sci. Pollut. Res. **30**(22), 61411–61429 (2023)

4. W. Azam, I. Khan, S.A. Ali, Alternative energy and natural resources in determining environmental sustainability: a look at the role of government final consumption expenditures in France. Environ. Sci. Pollut. Res. **30**(1), 1949–1965 (2023)

5. S.S. Ali et al., Bioplastic production in terms of life cycle assessment: a state-of-the-art review. Environ. Sci. Ecotechnol. **15**, 100254 (2023)

6. M.M. Rahman et al., Powering agriculture: present status, future potential, and challenges of renewable energy applications. Renew. Energy **188**, 731–749 (2022)

7. A. Rahman, O. Farrok, M.M. Haque, Environmental impact of renewable energy source based electrical power plants: solar, wind, hydroelectric, biomass, geothermal, tidal, ocean, and osmotic. Renew. Sustain. Energy Rev. **161**, 112279 (2022)

8. B. Roose et al., Local manufacturing of perovskite solar cells, a game-changer for low-and lower-middle income countries? Energy Environ. Sci. **15**(9), 3571–3582 (2022)

9. U.S. Meda, Y.V. Rajyaguru, A. Pandey, Generation of green hydrogen using self-sustained regenerative fuel cells: opportunities and challenges. Int. J. Hydrogen Energy **48**, 28289–28314 (2023)

10. V.M. Avargani et al., A comprehensive review on hydrogen production and utilization in North America: prospects and challenges. Energy Convers. Manage. **269**, 115927 (2022)

11. M. Gopinath, R. Marimuthu, A review on solar energy-based indirect water-splitting methods for hydrogen generation. Int. J. Hydrogen Energy **47**(89), 37742–37759 (2022)

12. P. Pattanayak et al., Recent progress in perovskite transition metal oxide-based photocatalyst and photoelectrode materials for solar-driven water splitting. J. Environ. Chem. Eng. **10**, 108429 (2022)

13. A.R. Fareza et al., Nanoscale metal oxides–2D materials heterostructures for photoelectrochemical water splitting—a review. J. Mater. Chem. A **10**(16), 8656–8686 (2022)

14. M. Nasser, H. Hassan, Assessment of hydrogen production from waste heat using hybrid systems of Rankine cycle with proton exchange membrane/solid oxide electrolyzer. Int. J. Hydrogen Energy **48**(20), 7135–7153 (2023)

15. Y. Wu et al., Recent progress in biomass-derived nanoelectrocatalysts for the sustainable energy development. Fuel **323**, 124349 (2022)

16. A.P. Demchenko, Proton transfer reactions: from photochemistry to biochemistry and bioenergetics. BBA Adv. **3**, 100085 (2023)

17. H. Jing et al., Theory-oriented screening and discovery of advanced energy transformation materials in electrocatalysis. Adv. Powder Mater. **1**(1), 100013 (2022)

18. N.A. Kamaruzaman et al., Recent advances in transition metals-based materials as electrocatalysts for water splitting. Int. J. Electrochem. Sci. **18**, 100187 (2023)

19. M. Ďurovič, J. Hnát, K. Bouzek, Electrocatalysts for the hydrogen evolution reaction in alkaline and neutral media. A comparative review. J. Power. Sources **493**, 229708 (2021)

20. E. Loni, A. Shokuhfar, M. Siadati, Cobalt-based electrocatalysts for water splitting: an overview. Catal. Surv. Asia **25**, 114–147 (2021)

21. X. Zhang, L. Wang, H. Fu, Recent advances in rechargeable Zn-based batteries. J. Power. Sources **493**, 229677 (2021)

22. M.U. Nisa et al., CdSe supported SnO₂ nanocomposite with strongly hydrophilic surface for enhanced overall water splitting. Fuel **321**, 124086 (2022)

23. A.G. Abid et al., Stainless steel supported NiS/CeS nanocomposite for significantly enhanced oxygen evolution reaction in alkaline media. J. Solid State Electrochem. **26**(10), 2107–2118 (2022)

24. Z. Chen et al., Controllable design of nanoworm-like nickel sulfides for efficient electrochemical water splitting in alkaline media. Mater. Today Energy **18**, 100573 (2020)

25. A. Farhan et al., Transition-metal sulfides with excellent hydrogen and oxygen reactions: a mini-review. J. Solid State Chem. **329**, 124445 (2023)

26. S.K. Ramesh, V. Ganesan, J. Kim, FeSe2-CoSe2/CoSe2 yolk-shell nanoboxes as superior electrocatalysts for the oxygen evolution reaction. Mater. Lett. **323**, 132573 (2022)

27. K. Wang et al., Selenide/sulfide heterostructured NiCo2Se4/NiCoS4 for oxygen evolution reaction, hydrogen evolution reaction, water splitting and Zn-air batteries. Electrochim. Acta **368**, 137584 (2021)

28. J. Yang et al., Metal-organic framework-derived FeS2/CoNiSe2 heterostructure nanosheets for highly-efficient oxygen evolution reaction. Appl. Surf. Sci. **578**, 152016 (2022)

29. A. Raveendran, M. Chandran, R. Dhanusuraman, A comprehensive review on the electrochemical parameters and recent material development of electrochemical water splitting electrocatalysts. RSC Adv. **13**(6), 3843–3876 (2023)

30. J. Li et al., Optimizing hydrogen production by alkaline water decomposition with transition metal-based electrocatalysts. Environ. Chem. Lett. **31**, 2583–2617 (2023)

31. X. Guan et al., Probing the national development from heavy metals contamination in river sediments. J. Clean. Prod. **419**, 138164 (2023)

32. S. Vignesh, H. Kim, Influence of molybdenum on Co3O4 coupled N-doped reduced graphene oxide composite for improved electrocatalytic alkaline oxygen evolution reaction: stability and mechanism insights. Int. J. Hydrogen Energy **48**, 37234–37247 (2023)

33. X. Yang et al., Heterogeneous ultra-thin FeCo-LDH@ Co (OH) 2 nanosheets facilitated electrons transfer for oxygen evolution reaction. Chem. Eng. J. **472**, 145076 (2023)

34. G. Calzaferri et al., Multiple equilibria description of type H1 hysteresis in gas sorption isotherms of mesoporous materials. Mater. Chem. Phys. **296**, 127121 (2023)

35. Y. Wang et al., Investigation of photo (electro) catalytic water splitting to evolve H2 on Pt-g-C3N4 nanosheets. Int. J. Hydrogen Energy **47**(65), 28007–28018 (2022)

36. J. Jiang et al., Superwetting molybdenum-based sulfide/phosphide heterostructures for efficient water electrolysis and solar thermoelectricity self-powered hydrogen production. Appl. Surf. Sci. **631**, 157482 (2023)

37. H. Tong, Y. Jiang, L. Xia, Enhancing photoelectrochemical water oxidation activity of BiVO4 photoanode through the Co-catalytic effect of Ni (OH) 2 and carbon quantum dots. Int. J. Hydrogen Energy **48**, 36694–36706 (2023)

38. M. Liu et al., Construction of an electrode with hierarchical three-dimensional NiFe-oxyhydroxides by two-step electrodeposition for large-current oxygen evolution reaction. Int. J. Hydrogen Energy **51**, 626–637 (2023)

39. S. Bi et al., (Digital Presentation) The effects of sulfur-oxygen ratio at the heterogeneous interface on oxygen evolution reaction performance of Ni3S2@ Ni3Fe catalysts for alkaline water electrolysis. ECS Trans. **111**(4), 97 (2023)

40. Y. Sun et al., Deep neural network based battery impedance spectrum prediction using only impedance at characteristic frequencies. J. Power. Sources **580**, 233414 (2023)

41. S. Feng, et al., Self-assembled heterojunction CoSe2@ CoO catalysts for efficient seawater electrolysis. Electrochim. Acta **463**, 142870 (2023)

42. Y. Li et al., Effect of molybdenum phosphorus-based single/double-atom catalysts on hydrogen evolution reaction: first principles. Int. J. Hydrogen Energy **51**, 957–969 (2023)

43. N. Chen et al., Facile fabrication of flower-like CuS/MnCO3 microspheres clusters on nickel foam as an efficient bifunctional catalyst for overall water splitting. Int. J. Hydrogen Energy **46**(38), 19948–19961 (2021)

44. W. Li et al., Heterostructured CoSe2/FeSe2 nanoparticles with abundant vacancies and strong electronic coupling supported on carbon nanorods for oxygen evolution electrocatalysis. ACS Sustain. Chem. Eng. **8**(11), 4658–4666 (2020)

45. J.A. Rajesh et al., Bifunctional NiCo2Se4 and CoNi2Se4 nanostructures: efficient electrodes for battery-type supercapacitors and electrocatalysts for the oxygen evolution reaction. J. Ind. Eng. Chem. **79**, 370–382 (2019)

46. Y. Yang et al., An interfacial electron transfer on tetrahedral NiS2/NiSe2 heterocages with dual-phase synergy for efficiently triggering the oxygen evolution reaction. Small **16**(1), 1905083 (2020)

47. S. Ni et al., Interfacial engineering of the NiSe2/FeSe2 pp heterojunction for promoting oxygen evolution reaction and electrocatalytic urea oxidation. Appl. Catal. B **299**, 120638 (2021)

48. O.A. Oyetade, R.J. Kriek, NiSe-Ni3Se2/multiwalled carbon nanotube composites as efficient electrocatalysts for the oxygen evolution reaction in alkaline media. Electrocatalysis **11**, 35–45 (2020)

49. R. Bose et al., Self-supportive bimetallic selenide heteronanostructures as high-efficiency electro (pre) catalysts for water oxidation. ACS Sustain. Chem. Eng. **9**(38), 13114–13123 (2021)

50. X. Zhao et al., Electrical and structural engineering of cobalt selenide nanosheets by Mn modulation for efficient oxygen evolution. Appl. Catal. B **236**, 569–575 (2018)

51. G. Zhu et al., Nanocomposites based on CoSe2-decorated FeSe2 nanoparticles supported on reduced graphene oxide as high-performance electrocatalysts toward oxygen evolution reaction. ACS Appl. Mater. Interfaces **10**(22), 19258–19270 (2018)

52. S. Sadiq et al., Synergistic modification of end groups in Quinoxaline fused core-based acceptor molecule to enhance its photovoltaic characteristics for superior organic solar cells. J. Mol. Graph. Model. **123**, 108518 (2023)

Authors and Affiliations

Ali Junaid[1] · Muhammad Abdullah[2] · Nigarish Bano[1] · Faiqa Noreen[1] · Syed Imran Abbas Shah[1] · Razan A. Alshgari[1] · Saikh Mohammad[3] · Sumaira Manzoor[1] · Muhammad Fahad Ehsan[4] · Muhammad Naeem Ashiq[1]

✉ Muhammad Naeem Ashiq
naeembzu@bzu.edu.pk

1   Institute of Chemical Sciences, Bahauddin Zakariya University, Multan 60800, Pakistan

2   Department of Chemistry, Government College University, Lahore, Pakistan

3   Department of Chemistry, College of Science, King Saud University, 11451 Riyadh, Saudi Arabia

4   Department of Civil and Environmental Engineering, Northeastern University, Boston 02115 MA, USA